

Bulk Superconductivity up to 122 K in the Tl-Pb-Sr-Ca-Cu-O System

M. A. SUBRAMANIAN, C. C. TORARDI, J. GOPALAKRISHNAN, P. L. GAI, J. C. CALABRESE, T. R. ASKEW, R. B. FLIPPEN, A. W. SLEIGHT

New high-temperature superconductors based on oxides of thallium and copper, but not containing barium, have been prepared. A transition temperature (T_c) of about 85 K is found for $(\text{Tl}_{0.5}\text{Pb}_{0.5})\text{Sr}_2\text{CaCu}_2\text{O}_7$, whereas $(\text{Tl}_{0.5}\text{Pb}_{0.5})\text{Sr}_2\text{Ca}_2\text{Cu}_3\text{O}_9$ has a T_c of about 120 K. Both materials possess tetragonal symmetry with $a = 3.80 \text{ \AA}$, $c = 12.05 \text{ \AA}$ for $(\text{Tl}_{0.5}\text{Pb}_{0.5})\text{Sr}_2\text{CaCu}_2\text{O}_7$, and $a = 3.81 \text{ \AA}$, $c = 15.23 \text{ \AA}$ for $(\text{Tl}_{0.5}\text{Pb}_{0.5})\text{Sr}_2\text{Ca}_2\text{Cu}_3\text{O}_9$. A structure refinement of the latter phase has been carried out with single-crystal x-ray diffraction data.

THE DISCOVERY OF SUPERCONDUCTIVITY in the Tl-Ba-Ca-Cu-O system (1) has led to the identification of two homologous series of superconducting copper oxides, $\text{Tl}_2\text{Ba}_2\text{Ca}_{n-1}\text{Cu}_n\text{O}_{2n+4}$ (2-4) and $\text{TlBa}_2\text{Ca}_{n-1}\text{Cu}_n\text{O}_{2n+3}$ (5-7) where n is the number of adjacent Cu-O layers. For both cases, the transition temperature increases with the number of Cu-O layers (n). Recently, Sheng *et al.* (8) reported superconductivity at 20 K (some samples with onset at 70 K) in the Tl-Sr-Ca-Cu-O system with a weak Meissner effect ($<1\%$). Our attempts to synthesize $\text{Tl}_2\text{Sr}_2\text{Ca}_{n-1}\text{Cu}_n\text{O}_{2n+4}$ ($n = 1, 2, \text{ and } 3$) and $\text{TlSr}_2\text{Ca}_{n-1}\text{Cu}_n\text{O}_{2n+3}$ ($n = 2 \text{ and } 3$) were not successful. In addition to the above compositions, we also tried numerous combinations by varying Tl:Sr:Ca:Cu ratios. A few samples showed a weak Meissner effect around 20 K but we did not find evidence for superconductivity above 20 K in any of the samples. In this paper we report on the observation of bulk superconductivity up to 122 K ($\geq 30\%$ Meissner fraction and zero resistivity at 115 K) in the system Tl-Pb-Sr-Ca-Cu-O. We have identified at least two superconducting phases by x-ray and electron diffraction studies. We have also grown single crystals of one of the phases whose composition can be approximated as $(\text{Tl,Pb})\text{Sr}_2\text{Ca}_2\text{Cu}_3\text{O}_x$ and determined its crystal structure.

Compositions in the Tl-Pb-Sr-Ca-Cu-O system were prepared by reacting Tl_2O_3 , CaO_2 , SrO_2 , PbO_2 , and CuO in various proportions at 850° to 915°C in sealed gold tubes for 3 to 12 hours. Powder x-ray diffraction revealed that most of the products were mixtures containing mainly two

phases with characteristic reflections at 12.1 \AA and 15.2 \AA . Flux exclusion measurements showed superconductivity in all samples prepared in the system Tl-Pb-Sr-Ca-Cu-O. Meissner fractions were large ($\geq 30\%$) and transition temperatures were 80 to 90 K

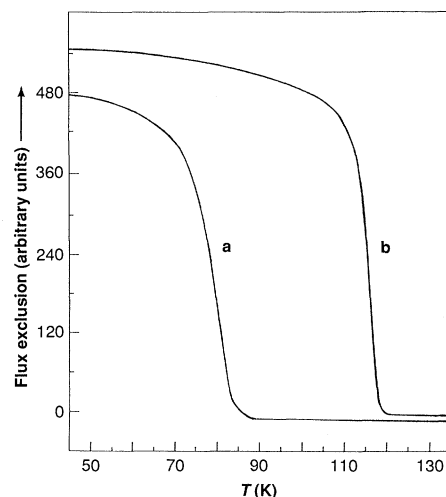


Fig. 1. Magnetic flux exclusion data: curve a, $(\text{Tl,Pb})\text{Sr}_2\text{CaCu}_2\text{O}_x$; and curve b, $(\text{Tl,Pb})\text{Sr}_2\text{Ca}_2\text{Cu}_3\text{O}_x$.

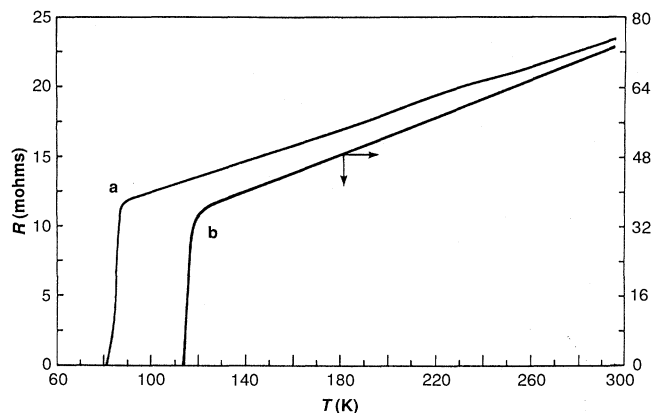


Fig. 2. Electrical resistivity data for polycrystalline samples: curve a, $(\text{Tl,Pb})\text{Sr}_2\text{CaCu}_2\text{O}_x$; and curve b, $(\text{Tl,Pb})\text{Sr}_2\text{Ca}_2\text{Cu}_3\text{O}_x$.

in some samples and 115 to 122 K in others. However, when we excluded any one of the metal components, no superconductivity was observed. By combining x-ray and Meissner data, we conclude that the 12.1 \AA phase has a superconducting transition temperature (T_c) of 80 to 90 K whereas the phase with 15.2 \AA has a T_c around 120 K. This suggested that these phases are probably similar to $\text{TlBa}_2\text{CaCu}_2\text{O}_7$ and $\text{TlBa}_2\text{Ca}_2\text{Cu}_3\text{O}_9$. Figure 1 shows the Meissner data, and Fig. 2 shows the resistivity plot for two polycrystalline samples, one of which contained predominantly the 15.2 \AA phase and the other containing the 12.1 \AA material.

Single crystals of the 15.2 \AA phase were grown from an oxide mixture in the molar ratio 1:1:2:3:4 (Tl:Pb:Sr:Ca:Cu) in a sealed gold tube. The mixture was heated to 910°C for 6 hours and cooled at 2°C per minute. Plate-like crystals found in the melt were separated and used for further characterization and structure determination. Flux-exclusion measurement on these crystals showed a sharp superconducting transition at 118 K. Single crystal x-ray and microprobe analysis (given below) indicated that the Sr and Ca sites are close to being fully occupied and that the Tl:Pb ratio is approximately 1:1. Thus, we conclude that the substitution of Pb for Tl in the lattice stabilizes the $(\text{Tl,Pb})\text{Sr}_2\text{Ca}_{n-1}\text{Cu}_n\text{O}_x$ ($n = 2 \text{ and } 3$) phases. Compounds in the solid solution $(\text{Tl}_{1-y}\text{Pb}_y)\text{Sr}_2\text{Ca}_{n-1}\text{Cu}_n\text{O}_x$ ($n = 2, 3$) were synthesized for various values of y . Results show that single-phase materials are obtained for both n values when y is close to 0.5. All the lines in the x-ray powder diffraction patterns for $(\text{Tl}_{0.5}\text{Pb}_{0.5})\text{Sr}_2\text{CaCu}_2\text{O}_x$ and $(\text{Tl}_{0.5}\text{Pb}_{0.5})\text{Sr}_2\text{Ca}_2\text{Cu}_3\text{O}_x$ could be indexed on the basis of primitive tetragonal unit cells with $a = 3.80 \text{ \AA}$ and $c = 12.05 \text{ \AA}$, and $a = 3.81 \text{ \AA}$ and $c = 15.23 \text{ \AA}$, respectively. Figure 3 shows the x-ray powder diffraction patterns of these phases.

Electron microscopy and related microanalytical techniques were used for microstruc-

Central Research and Development Department, E. I. du Pont de Nemours and Company, Experimental Station, Wilmington, DE 19880.

tural and microchemical characterization. The studies showed plate-like crystals of dimensions varying from 10 μm to 40 μm and some with dimensions of tens of micrometers (100 μm to 150 μm). Scanning electron microscopy (SEM) and microprobe analysis from the bulk material indicated that the plates contained lead. Microanalysis was also carried out on the same single crystal (measuring $\sim 100 \mu\text{m}$ by $90 \mu\text{m}$) used for the x-ray diffraction study. The crystal plate was carefully glued to the holder for microanalytical characterization. A Tl:Pb ratio of approximately 1:1 was detected in the plate. Some local variations in cation ratios, in particular Sr:Ca, were observed when analyzed across the single plate. The results were consistent with microchemical analyses using a Vacuum Generators, Inc., model HB501 Scanning Transmission Electron Microscope (VG STEM) on crushed material.

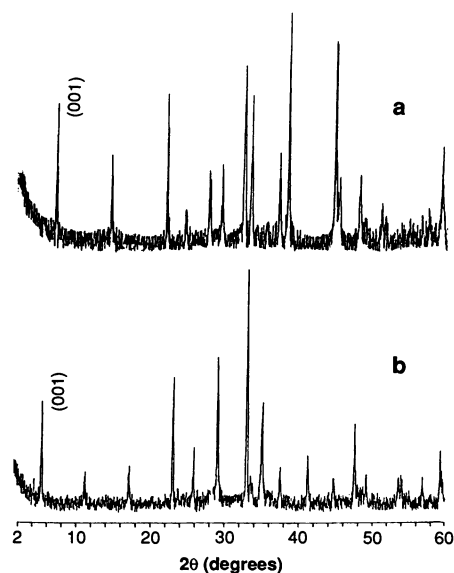


Fig. 3. X-ray powder diffraction patterns: (a) $(\text{Tl}_{0.5}\text{Pb}_{0.5})\text{Sr}_2\text{CaCu}_2\text{O}_x$; and (b) $(\text{Tl}_{0.5}\text{Pb}_{0.5})\text{Sr}_2\text{Ca}_2\text{Cu}_3\text{O}_x$.

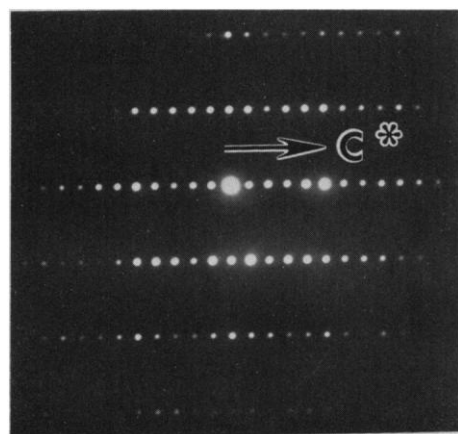


Fig. 4. Electron diffraction pattern of $(\text{Tl,Pb})\text{Sr}_2\text{Ca}_2\text{Cu}_3\text{O}_x$ in $[010]$ orientation (with primitive tetragonal cell $\sim 3.8 \text{ \AA}$ by 15 \AA).

The crystal fragments were supported on carbon grids and examined by electron microscopy using a Philips CM12 instrument. The electron diffraction pattern from the plates indicated a tetragonal basic cell with $a \approx 3.8 \text{ \AA}$ and $c \approx 15 \text{ \AA}$ (Fig. 4), and the images indicated a layered structure containing triple Cu-O perovskite layers (Fig. 5). Several of the crystals examined exhibited stacking faults and intergrowths of $\sim 12 \text{ \AA}$ suggesting variation in chemical composition.

Single-crystal x-ray diffraction data are summarized in Table 1. Atomic positions were taken from the structure of $\text{TlBa}_2\text{Ca}_2\text{Cu}_3\text{O}_9$ (7). The structure was refined by full-matrix least-squares analysis with neutral atom scattering factor curves and anomalous scattering terms and anisotropic thermal motion for the metal atoms. Because the scattering factor curves of Tl and Pb are very similar, it is not possible to differentiate between these two atoms in the structure. Occupation factors of the Tl/Pb and Sr atoms were refined and both sites were

found to be fully occupied: 1.00(1) and 0.98(1) atom per site, respectively (last-digit uncertainty in parentheses). The occupancy factor for the Ca site was high, indicating substitution of $\sim 20\%$ Sr similar to that found in $(\text{Sr,Ca})\text{CuO}_2$ (9) and $\text{Bi}_2\text{Sr}_{3-x}\text{Ca}_x\text{Cu}_2\text{O}_8$ (10), or $\sim 6\%$ Tl/Pb similar to the situation observed in $\text{TlBa}_2\text{Ca}_2\text{Cu}_3\text{O}_9$ (7), $\text{Tl}_2\text{Ba}_2\text{CaCu}_2\text{O}_8$ (3), and $\text{Tl}_2\text{Ba}_2\text{Ca}_2\text{Cu}_3\text{O}_{10}$ (2). When on their ideal sites, large thermal motion was seen for the Tl/Pb atoms, $B_{11} = 5.0(1)$ and $B_{33} = 1.1(1) \text{ \AA}^2$, and for the oxygen atom in the thallium-lead sheets, $\text{O}(4)$, $B = 8(1) \text{ \AA}^2$. Features such as these are seen in all of the Tl-containing copper-based high T_c oxides (2, 3, 7, 11, 12) and suggest that the intrasheet Tl/Pb and O atoms are actually displaced from their ideal positions in order to form a more favorable bonding environment, and that an average structure is seen with tetragonal symmetry. This environment was modeled by refining both Tl/Pb(1) and O(4) in the $4l(x,0,0)$ and $4n(x,1/2,0)$ sites, respectively, to give a statistically disordered fourfold arrangement

Table 1. Summary of crystallographic information for $(\text{Tl,Pb})\text{Sr}_2\text{Ca}_{1.9}\text{Cu}_3\text{O}_9$. Last-digit uncertainty is in parentheses.

Sample dimensions (mm)	$0.10 \times 0.09 \times 0.02$
Diffractometer	Enraf-Nonius CAD4
Radiation	Mo $K\alpha$
Monochromator	Graphite
Formula weight	812.4 ($\text{Tl}_{0.55}\text{Pb}_{0.55}\text{Sr}_2\text{Ca}_{1.9}\text{Cu}_3\text{O}_9$)
Crystal system	Tetragonal
Space group	$P4/mmm$ (no. 123)
Cell constants (\AA)	$a = 3.808(1)$, $c = 15.232(7)$
Temperature	Ambient
Calculated density (g cm^{-3})	6.10 ($Z = 1$)
Scan mode	ω
2θ range	0 to 70 degrees
Octants	+++ , -++ , --- , +-+
Absorption coefficient μ (cm^{-1})	404.9
Absorption correction	Analytical
Transmission factors	0.058 to 0.390
Extinction parameter (mm)	$1.2(2) \times 10^{-5}$
Total reflections	2068
Independent reflections	216 ($I > 3\sigma$)
Data per parameters	8.6
R	0.048
R_w	0.047

Table 2. Positional [space group $P4/mmm$ (no. 123)] and thermal parameters for the atoms of $(\text{Tl,Pb})\text{Sr}_2\text{Ca}_{1.9}\text{Cu}_3\text{O}_9$. All metal atoms were refined with anisotropic thermal parameters. The equivalent isotropic thermal parameter is marked with a prime sign.

Atom	Site	x	y	z	B (\AA^2)
Tl/Pb(1)*	4l	0.067(3)	0.00	0.00	1.8(2)'
Sr(1)	2h	0.50	0.50	0.1709(2)	1.6(1)'
Cu(1)	1b	0.00	0.00	0.50	1.2(1)'
Cu(2)	2g	0.00	0.00	0.2868(2)	1.1(1)'
Ca(1)†	2h	0.50	0.50	0.3928(3)	1.5(1)'
O(1)	2e	0.00	0.50	0.50	1.2(3)
O(2)	4i	0.00	0.50	0.2924(7)	1.5(2)
O(3)	2g	0.00	0.00	0.1311(11)	1.6(3)
O(4)*	4n	0.60(2)	0.50	0.00	3.2(14)

*Refined off of the ideal site.

†Site composition fixed at 0.94 Ca + 0.06 Tl/Pb.

around the ideal sites. Note, however, that shifting these atoms to the $4j$ ($x, x, 0$) sites gave an equally good refinement with identical R factors. The largest peak in a difference Fourier map was 0.38 electrons per angstrom cubed. Positional and thermal parameters are given in Tables 2 and 3. Inter-

Table 3. Anisotropic thermal parameters (\AA^2) for the metal atoms of $(\text{Tl,Pb})\text{Sr}_2\text{Ca}_{1.9}\text{Cu}_3\text{O}_9$. Parameters are given by the expression $\exp[-0.25(B_{11}h^2a^2 + \dots + 2(B_{12}hka^*b^* \dots))]$; $B_{12} = B_{13} = B_{23} = 0.0$.

Atom	B_{11}	B_{22}	B_{33}
Tl/Pb(1)	2.1(4)	2.0(3)	1.06(5)
Sr(1)	1.5(1)	1.5	1.8(1)
Cu(1)	1.0(1)	1.0	1.7(1)
Cu(2)	0.9(1)	0.9	1.6(1)
Ca(1)	1.6(2)	1.6	1.5(1)

Table 4. Interatomic distances (\AA) and angles (degrees) in $(\text{Tl,Pb})\text{Sr}_2\text{Ca}_{1.9}\text{Cu}_3\text{O}_9$. Last-digit uncertainty in parentheses. The last column represents the number of times each bond distance or angle occurs around the metal or central atom.

Distances		
Cu(1)-O(1)	1.9040(5)	($\times 4$)
Cu(2)-O(2)	1.9059(7)	($\times 4$)
Cu(2)-O(3)	2.37(2)	($\times 1$)
Cu(1)-Cu(2)	3.248(3)	(intersheet)
Tl/Pb(1)-O(3)	2.01(2)	($\times 2$)
Tl/Pb(1)-O(4)	2.23-3.19	($\times 4$)
Sr(1)-O(2)	2.655(7)	($\times 4$)
Sr(1)-O(3)	2.760(4)	($\times 4$)
Sr(1)-O(4)	2.633(11)	($\times 1$)
Ca(1)-O(1)	2.509(3)	($\times 4$)
Ca(1)-O(2)	2.442(7)	($\times 4$)
Angles		
O(1)-Cu(1)-O(1)	180.0	($\times 2$)
O(1)-Cu(1)-O(1)	90.0	($\times 4$)
Cu(1)-O(1)-Cu(1)	180.0	($\times 1$)
O(2)-Cu(2)-O(2)	174.9(7)	($\times 2$)
O(2)-Cu(2)-O(2)	89.89(2)	($\times 4$)
O(2)-Cu(2)-O(3)	92.6(4)	($\times 4$)
Cu(2)-O(2)-Cu(2)	174.9(7)	($\times 1$)

atomic distances and angles are listed in Table 4.

The crystal structure of $(\text{Tl,Pb})\text{Sr}_2\text{Ca}_2\text{Cu}_3\text{O}_9$ is essentially the same as that of $\text{TlBa}_2\text{Ca}_2\text{Cu}_3\text{O}_9$ (5, 7), and is closely related to that of $\text{Tl}_2\text{Ba}_2\text{Ca}_2\text{Cu}_3\text{O}_{10}$ (2). Triple sheets of corner-sharing CuO_4 groups are oriented parallel to the (001) plane (Fig. 6). The middle sheet is exactly planar and the CuO_4 units have $4/mmm$ (D_{4h}) site symmetry. The Cu(1)-O(1) bond length in this layer is 1.904 \AA whereas that in the outer CuO_2 layers is 1.906 \AA because of a slight puckering of these layers. Additional oxygen atoms are bonded to the copper atoms of the two outer sheets at a distance of 2.37 \AA giving these copper atoms a square-pyramidal environment with $4mm$ (C_{4v}) symmetry. The intrasheet copper-oxygen bonds in the triple-layer unit of $(\text{Tl,Pb})\text{Sr}_2\text{Ca}_2\text{Cu}_3\text{O}_9$ are the shortest yet observed in any of the Tl-containing superconductors, and are to be compared to a value of approximately 1.93 \AA for the Tl-Ba materials (2, 3, 7, 11). Although the interlayer oxygen-oxygen separation is essentially the same for the double and triple copper-oxygen layers of the Tl-Ba-Ca and Tl-Sr-Ca phases, the interlayer Cu-Cu distance correlates with the length of the apical Cu-O bond of the square pyramids. As this bond distance decreases (2.73 to 2.37 \AA), the Cu-Cu distance increases (3.17 to 3.25 \AA). This, of course, also correlates with the degree of planarity of the outer Cu-O sheets. $(\text{Tl,Pb})\text{Sr}_2\text{Ca}_2\text{Cu}_3\text{O}_9$ exhibits the shortest apical Cu-O bond, 2.37 \AA , and the longest distance between the oxygen plane and the copper plane of the outer CuO_2 sheets, 0.085 \AA .

The triple Cu-O sheets of $(\text{Tl,Pb})\text{Sr}_2\text{Ca}_2\text{Cu}_3\text{O}_9$ are separated by calcium ions that bond to eight oxygen atoms at an average distance of 2.48 \AA as found in the structures of $\text{Tl}_2\text{Ba}_2\text{Ca}_{n-1}\text{Cu}_n\text{O}_{2n+4}$ ($n = 2, 3$),

12) and $\text{TlBa}_2\text{Ca}_2\text{Cu}_3\text{O}_9$ (7). Also analogous to the latter compounds is the substitution of $\sim 6\%$ of the calcium sites with Tl^{3+} or Pb^{4+} . [The ionic radii for Sr^{2+} and Pb^{2+} are larger than those of Tl^{3+} and Pb^{4+} , and appear to be less suitable for these sites, although Sr substitution for Ca is known to occur in $\text{Ca}_{0.86}\text{Sr}_{0.14}\text{CuO}_2$ (9) and $\text{Bi}_2\text{Sr}_{3-x}\text{Ca}_x\text{Cu}_2\text{O}_8$ (10).] Strontium ions reside above and below the copper-oxygen triple sheets in nine-coordination with oxygen. The average Sr-O bond length is 2.70 \AA and compares well with the sum of ionic radii (13), 2.71 \AA . It is significant that the strontium sites refine to full occupancy because it indicates that lead goes only into the Tl or Ca sites even though the ionic radii for Sr^{2+} and Pb^{2+} are similar, 1.31 and 1.35 \AA , respectively. However, it may be possible that the Sr sites are only partially occupied with strontium and enough Pb^{2+} to coincidentally result in the equivalent x-ray scattering power of a full Sr atom.

In comparison with $\text{Tl}_2\text{Ba}_2\text{Ca}_2\text{Cu}_3\text{O}_{10}$ (2), which possesses rock salt-like double thallium-oxygen sheets, $(\text{Tl,Pb})\text{Sr}_2\text{Ca}_2\text{Cu}_3\text{O}_9$ has single Tl/Pb-O sheets that alternately stack with the Sr-Cu-Ca-O slabs along the c axis. Single Tl-O layers and triple Cu-O layers are also found in $\text{TlBa}_2\text{Ca}_2\text{Cu}_3\text{O}_9$ (7). The Tl/Pb atoms of the new strontium phase

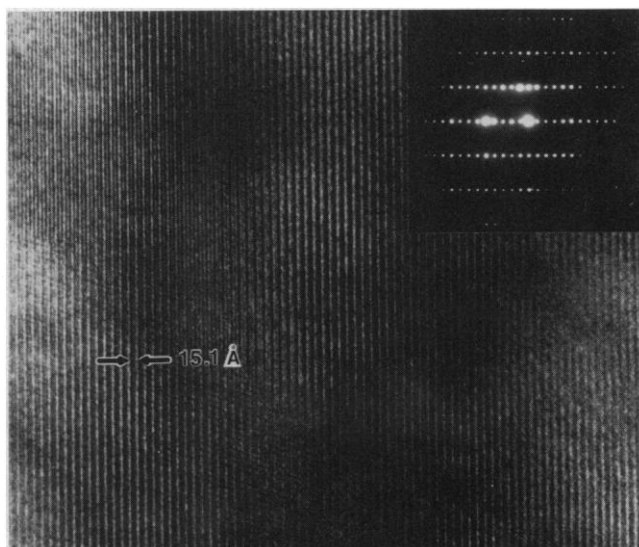


Fig. 5. Lattice image (low magnification) from the [010] $(\text{Tl,Pb})\text{Sr}_2\text{Ca}_2\text{Cu}_3\text{O}_x$ plate showing a layered structure with $\sim 15 \text{\AA}$ repeat spacing. Electron diffraction pattern in [010] orientation is inset.

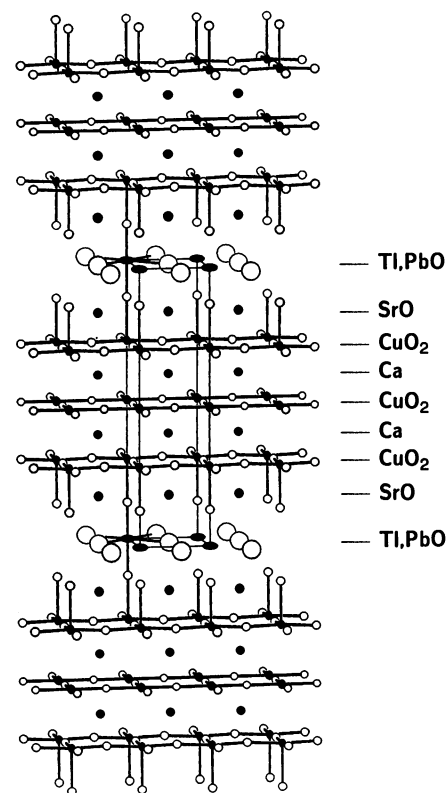


Fig. 6. The structure of $(\text{Tl,Pb})\text{Sr}_2\text{Ca}_2\text{Cu}_3\text{O}_9$. Atoms in the Tl,PbO layers are shown on their ideal positions. Metal atoms are shaded and Cu-O bonds are drawn.

are associated with six O atoms in a distorted octahedral arrangement when Tl/Pb(1) and O(4) are on their ideal sites. However, the existence of correlated atomic displacements within the thallium(lead)-oxygen sheets is suggested by the apparent disordered arrangement in the average tetragonal structure. When shifted off of these sites (Table 2), intralayer Tl/Pb-O distances can range from 2.23 to 3.19 Å whereas two short Tl/Pb-O distances remain above and below Tl/Pb. Analogous situations are found in all of the thallium-containing copper-oxide superconductors. The atomic displacements give rise to local chains or pairs of Tl/Pb and O atoms, and this could create an atomic modulation along the a_1 and a_2 axes (14, 15).

Two oxidation states would normally be considered for lead, Pb^{2+} and Pb^{4+} . The partial replacement of Tl^{3+} by Pb in $(Tl,Pb)Sr_2Ca_{n-1}Cu_nO_{2n+3}$ phases would then cause the Cu oxidation state to increase for Pb^{2+} or to decrease for Pb^{4+} . Although some Cu^{3+} would remain for the $(Tl_{0.5}Pb_{0.5})Sr_2^{+}Ca_2^{+}Cu_{2.5}^{+}Cu_{0.5}^{+}O_9$ formulation, its concentration seems rather low for a 122 K superconductor. However, it is

likely that the 6s band, composed of Tl 6s, Pb 6s, and O 2p states, crosses the Fermi level thereby creating more Cu^{3+} than this formulation would suggest. Work is under way to establish the actual carrier concentration in these new high T_c superconductors containing Tl and Cu.

REFERENCES AND NOTES

1. Z. Z. Sheng and A. M. Hermann, *Nature* **332**, 138 (1988).
2. C. C. Torardi *et al.*, *Science* **240**, 631 (1988).
3. M. A. Subramanian *et al.*, *Nature* **332**, 420 (1988).
4. S. S. P. Parkin *et al.*, *Phys. Rev. Lett.* **60**, 2539 (1988).
5. S. S. P. Parkin *et al.*, *ibid.* **61**, 750 (1988).
6. M. Hervieu *et al.*, *J. Solid State Chem.* **75**, 212 (1988).
7. M. A. Subramanian *et al.*, *ibid.*, in press.
8. Z. Z. Sheng *et al.*, in preparation.
9. T. Siegrist *et al.*, *Nature* **334**, 231 (1988).
10. M. A. Subramanian *et al.*, *Science* **239**, 1015 (1988).
11. C. C. Torardi *et al.*, *Phys. Rev. B* **38**, 225 (1988).
12. D. E. Cox *et al.*, *Phys. Rev. B*, in press.
13. R. D. Shannon, *Acta Crystallogr.* **A32**, 751 (1976).
14. J. D. FitzGerald, *Phys. Rev. Lett.* **60**, 2797 (1988).
15. A. W. Hewat, E. A. Hewat, J. Brynstad, H. A. Mook, E. D. Specht, *Physica C* **152**, 438 (1988).
16. We thank P. M. Kelly, C. R. Walther, R. A. Oswald, W. J. Marshall, L. Cooke, D. Groski, G. M. Hyatt, C. M. Foris, E. Boyes, D. L. Smith, I. R. Hartmann, and C. B. Michel for their assistance.

26 August 1988; accepted 16 September 1988

The Paleomagnetic Field from Equatorial Deep-Sea Sediments: Axial Symmetry and Polarity Asymmetry

DAVID A. SCHNEIDER AND DENNIS V. KENT

Paleomagnetic data from 89 equatorial deep-sea sediment cores indicate that the configuration of the time-averaged geomagnetic field depends strongly on polarity state but that it remains within 1 degree of axial symmetry throughout the Pliocene and Pleistocene (last 5 million years). The relative magnitude of the nondipole field was greater by almost a factor of 2 during reverse than during normal polarity intervals. These results thus support earlier suggestions that there may be a standing (nonreversing) component of the geomagnetic dynamo.

THE TIME-AVERAGED GEOMAGNETIC field can deviate from the field of a geocentric axial dipole (1). Although the difference is small, amounting to a few degrees, the deviation, attributed to a long-term nondipole field (NDF), provides a means to examine the nature of the underlying dynamo.

One intriguing aspect of the NDF is its apparent dependence on polarity state. Indications of this dependence have come, for example, from Wilson's (1) examination of piston core data (2) and also from his study of paleomagnetic data from the U.S.S.R.

(3). Also, Merrill and McElhinny (4), using a spherical harmonic analysis of global paleomagnetic data, showed that the dominant NDF terms (the axial quadrupole and axial octupole) are larger by nearly a factor of 2

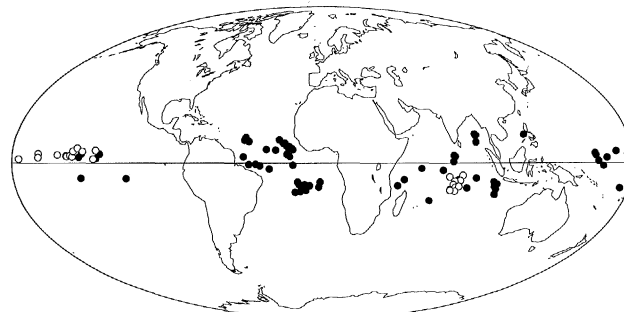
for reverse than for normal polarity data. These results, although suggestive of polarity dependence, were open to alternative explanation: the limited age control allowed that differences between normal and reverse directions might result from changes in the NDF with time and be fundamentally unrelated to polarity.

We have studied these possible NDF effects in well-dated Pliocene to Pleistocene deep-sea sediment cores from equatorial latitudes (all but one within $\pm 15^\circ$). Near the equator, the axial quadrupole NDF is greatest and paleomagnetic directions close to horizontal and thus are least susceptible to spurious shallowing caused by sedimentary inclination error. Pelagic sediments are known to provide high-quality paleomagnetic data (5) and can be used to study the time-averaged properties of the field because bioturbation and the low sedimentation rates (about 1 cm per 1000 years) act to average secular variation.

In an earlier study of 29 piston cores from the equatorial Indian Ocean (6), we concluded that the NDF was different during the Brunhes [0 to 0.73 Ma (million years ago); normal polarity] from that during the Matuyama (0.73 to 2.47 Ma; reverse polarity) interval. Resolution in the earlier Gauss (2.47 to 3.40 Ma; normal polarity) and Gilbert (3.40 to 5.35 Ma; reverse polarity) chrons was poor, and therefore the supposed polarity dependence could not be adequately tested. In this report, we present data from an expanded set of deep-sea sediment cores (60 additional cores for a total of 89) taken from the Indian, Atlantic, and Pacific oceans (Fig. 1). By studying cores distributed around the equatorial region, we could describe better the axial quadrupole field and also test whether the dipole axis was inclined to the rotation axis, that is, whether the paleomagnetic field was axially symmetric. The deep-sea sediments studied were recovered with standard piston coring techniques. Data for 29 of the 89 cores are in (6); tabulated data for the remaining cores are available from the authors (7).

Because none of the cores were oriented in azimuth, we could not determine absolute

Fig. 1. Location of the 89 equatorial deep-sea sediment cores used in this study. Closed circles show cores containing only Brunhes or Matuyama age sediments, or both (that is, younger than 2.47 Ma). Open circles show cores also containing Gauss or Gilbert age sediments, or both (older than 2.47 Ma).



Lamont-Doherty Geological Observatory and Department of Geological Sciences, Columbia University, Palisades, NY 10964.